

A phase-dependent view of cyclotron lines from model accretion mounds on neutron stars

Dipanjana Mukherjee^{*} and Dipankar Bhattacharya^{*}

Inter-University Centre for Astronomy & Astrophysics, Post Bag 4, Ganeshkhind, Pune 411007, India

Accepted 2011 October 26. Received 2011 October 25; in original form 2011 June 21

ABSTRACT

In this paper we make a phase-dependent study of the effect of the distortion of the local magnetic field due to confinement of the accreted matter in X-ray pulsars on the cyclotron spectra emitted from the hotspot. We have numerically solved the Grad–Shafranov equation for axisymmetric static magnetohydrodynamic (MHD) equilibria of the matter confined at the polar cap of neutron stars. From our solution, we model the cyclotron spectra that will be emitted from the region, using a simple prescription and integrating over the entire mound. Radiative transfer through the accretion column overlying the mound may significantly modify the spectra in comparison to those presented here. However, we ignore this in the present paper in order to expose the effects directly attributable to the mound itself. We perform a spin phase-dependent analysis of the spectra to study the effect of the viewing geometry.

Key words: accretion, accretion discs – line: formation – magnetic fields – radiation mechanisms: non-thermal – binaries: general – X-rays: binaries.

1 INTRODUCTION

Neutron stars in high-mass X-ray binaries have high magnetic fields ($\sim 10^{12}$ G) and accrete matter from their companion stars either via stellar winds or by disc accretion. Magnetospheric interaction with the accretion flow causes the matter to be channelled to the magnetic poles, forming accretion columns (see e.g. Ghosh, Pethick & Lamb 1977; Ghosh & Lamb 1978; Koldoba et al. 2002; Romanova et al. 2003). The infalling plasma, with initial relativistic infall velocities, passes through an accretion shock at a height of a few kilometres from the neutron star surface and then settles down to a gradually slowing subsonic flow (Brown & Bildsten 1998; Cumming, Zweibel & Bildsten 2001).

Such X-ray binary systems show characteristic cyclotron resonance scattering features (CRSFs) in their spectra resulting from resonant scattering of radiation by electrons in the presence of a strong magnetic field (for discussion on theory and observation of cyclotron scattering features see e.g. Harding & Preece 1987; Araya & Harding 1999; Araya-Góchez & Harding 2000; Schönherr et al. 2007 and Mihara et al. 2007). In the immediate post-shock region the flow velocities are still relativistic ($\sim 0.16c$ for $\gamma = 5/3$ gas) and the plasma is optically thin to cyclotron scattering. As the accreted plasma descends and cools, it forms at the base a static mound confined by the magnetic field, and becomes optically thick to cyclotron scattering. Any distortion of the magnetic field in the mound due to pressure from the confined plasma will be reflected in the spectra emitted from the boundary of this region.

The nature and variation of the cyclotron spectra can give important clues regarding the properties of the emission region. Many systems show variations of line energies of the CRSF with the phase of rotation, e.g. Vela X-1, Her X-1, 4U 0115+63 and GX 301–2. This can be due to the variation of the local magnetic field structure at one or both poles as a line of sight (LOS) moves across the neutron star. Apart from the spin phase dependence, the cyclotron spectra are also seen to depend on the luminosity state of the system. Some systems such as V0332+53 (Tsygankov, Lutovinov & Serber 2010) show a negative correlation between luminosity and cyclotron line energy while some such as Her X-1 (Staubert et al. 2007) show a positive correlation. Such dependence of the line energy with change in accretion rate suggests a change of the local geometry or magnetic field structure. Some sources (e.g. 4U 1538–52, A 0535+26 and V0332+53) show multiple absorption features with anharmonic separation which can be due to a distortion of the local field from the dipolar magnetic field (Nishimura 2005, 2011).

In this paper we examine the effect on the cyclotron spectra arising from the distortion of the local magnetic field caused by the confined plasma. We consider an accreted mound in a static equilibrium confined by the magnetic field at the magnetic pole of a neutron star. We construct the equilibrium solution by solving the Grad–Shafranov equation. We do not consider the effects of continued accretion in this paper. We model the X-ray-emitting hotspot as a mound of accreted matter with finite height and no atmosphere. The Grad–Shafranov equation for the accreted matter on the neutron star poles has previously been solved by other authors, e.g. Hameury et al. (1983), Brown & Bildsten (1998), Litwin, Brown & Rosner (2001), Melatos & Phinney (2001), Payne & Melatos (2004, hereafter PM04), Payne & Melatos (2007) and Vigelijs & Melatos

^{*}E-mail: dipanjana@iucaa.ernet.in (DM); dipankar@iucaa.ernet.in (DB)

(2008), whose main aim was to study the extent of deformation and stability of the confined mound and also to deduce the effects of magnetic screening on the dipole moment of a neutron star. In this paper we extend this body of work to predict the cyclotron spectra emanating from such mounds.

We adopt a geometry similar to that used by Hameury et al. (1983), Brown & Bildsten (1998) and Litwin et al. (2001) and a numerical algorithm similar to the one developed by Mouschovias (1974) and PM04 for solving the Grad–Shafranov equation. However our treatment differs from PM04 in several aspects. We work in an axisymmetric cylindrical coordinate system instead of the spherical coordinate system of PM04. We use a polytropic equation of state for the accreted gas instead of the isothermal equation of state of PM04. Finally, we consider the mound to be strictly confined to the polar cap region, while PM04 allowed a significant amount of mass loading outside the polar cap.

We simulate the cyclotron spectra emitted from the accreted mound and perform a phase-resolved analysis of the emission. Our main objective in this paper is to perform a phase-dependent study of the effects of the accretion-induced distortion of the local magnetic field on the emergent spectra. In this work we do not perform a detailed radiative transfer calculation of CRSFs. Instead we use a Gaussian profile for the cyclotron feature originating from each point of the emission region, with the central line energy given by the magnetic field strength at that point, according to the well-known relativistic formula given by Sokolov & Ternov (1968). We also incorporate the effects of gravitational bending of light and finite energy resolution of detectors. We generate the resultant spectra by integrating over the entire mound, taking into account the variation of the field strength over the emitting region.

We structure the paper as follows. In Section 2 we first review the formulation of the Grad–Shafranov equation for the static magnetohydrodynamic (MHD) equilibria. We then outline the numerical algorithm adopted to solve the Grad–Shafranov equation and the test cases for verifying the code. In Section 3 we discuss the nature of the solutions obtained by solving the Grad–Shafranov equation and discuss the range of parameter space within which the valid solution can be obtained. Our results are indicative of the onset of MHD instabilities beyond this boundary. In Section 4 we describe the algorithm used to simulate the spectra from the mound and discuss the results from our simulation of the cyclotron absorption features. In Section 5 we summarize the results obtained from the simulations of the spectra and discuss the implications on observations of actual sources. The technical details of the geometrical construct used to compute the spectra are presented in Appendix B.

2 STATIC MHD EQUILIBRIA OF ACCRETED MATTER ON NEUTRON STAR POLES

In this work we consider a neutron star binary system where the magnetosphere cuts off the accretion disc at Alfvén radius (Ghosh et al. 1977; Ghosh & Lamb 1978) and matter is accreted on to the polar cap. We will consider a typical slowly spinning neutron star of mass $1.4 M_{\odot}$, radius $R = 10$ km and magnetic field $B = 10^{12}$ G (e.g. Bhattacharya & van den Heuvel 1991). A polar cap of radius $R_p = 1$ km will be considered corresponding to the footprint of dipole field lines that extend beyond a typical Alfvén radius of ~ 1000 km. Accreted matter is assumed to be confined within the polar cap region. We will consider the accreted matter to form a degenerate mound of finite height ($\simeq 100$ m or less) with a polytropic equation of state. We assume that the mound is in a steady-state equilibrium

supported by the magnetic field. We work in a cylindrical geometry (r, θ, z) with origin at the base of the polar cap (see Appendix B) and consider Newtonian gravity with constant acceleration (Hameury et al. 1983; Litwin et al. 2001):

$$\mathbf{g} = -1.86 \times 10^{14} \left(\frac{M_*}{1.4 M_{\odot}} \right) \left(\frac{R_s}{10 \text{ km}} \right)^{-2} \text{ cm s}^{-2} \hat{\mathbf{z}}. \quad (1)$$

The initial magnetic field (when no accreted matter is present) is dipolar. We approximate the dipolar field in the region by a uniform field along z : $\mathbf{B}_d = B_0 \hat{\mathbf{z}}$. We assume axisymmetry of the polar cap mound and use the ideal MHD equations, which may be cast in the form of the Grad–Shafranov equation. We solve this numerically to find the field and matter density configuration for the static equilibrium solution of the system.

2.1 Formulation of the Grad–Shafranov equation

For an axisymmetric system, one may decompose the magnetic field into a poloidal and a toroidal part:

$$\mathbf{B} = \mathbf{B}_p + \mathbf{B}_\theta = \frac{\nabla \psi \times \hat{\boldsymbol{\theta}}}{r}. \quad (2)$$

For our work we will assume $\mathbf{B}_\theta = 0$. The function $\psi(r, z)$ is the flux function which at a fixed r and z is proportional to the poloidal flux passing through a circle of radius r (see Kulsrud 2005; Biskamp 1993, for more discussion). The poloidal components of the magnetic field are

$$\mathbf{B}_r = -\frac{1}{r} \frac{\partial \psi}{\partial z}, \quad \mathbf{B}_z = \frac{1}{r} \frac{\partial \psi}{\partial r}. \quad (3)$$

Using equation (2) we can write the static Euler equation as

$$\nabla p - \rho \mathbf{g} + \frac{\Delta^2 \psi}{4\pi r^2} \nabla \psi = 0, \quad (4)$$

where Δ^2 is the Grad–Shafranov operator:

$$\Delta^2 = r \frac{\partial}{\partial r} \left(\frac{1}{r} \frac{\partial}{\partial r} \right) + \frac{\partial^2}{\partial z^2}.$$

Assuming an adiabatic gas $p = k_{\text{ad}} \rho^\gamma$, we separate the r and z components (Hameury et al. 1983; Litwin et al. 2001) by the method of characteristics (similar to PM04)

$$p_z - \rho g + \frac{\Delta^2 \psi}{4\pi r^2} \psi_z = 0, \quad p_r + \frac{\Delta^2 \psi}{4\pi r^2} \psi_r = 0, \quad (5)$$

where the subscripts indicate partial derivatives. Eliminating $\Delta^2 \psi / (4\pi r^2)$ from (5), we get the equation of the integral curve as

$$dz = -\frac{dr}{\psi_z / \psi_r} = -\frac{d\rho}{\rho g / c_s^2}, \quad (6)$$

where $c_s^2 = \gamma p / \rho$ is the adiabatic speed of sound. Solving the above two equations, we get $\psi = \text{constant}$ (which means the solutions are on constant ψ surfaces) and $gz + [\gamma p / (\gamma - 1) \rho] = f(\psi)$. Here, $f(\psi)$ is a ψ -dependent constant of integration. Rearranging the terms we can write the density as (Hameury et al. 1983)

$$\rho = A [Z_0(\psi) - z]^{\frac{1}{\gamma-1}}, \quad (7)$$

where $A = [g(\gamma - 1) / (\gamma k_{\text{ad}})]^{1/(\gamma-1)}$ is a constant. The function $Z_0(\psi)$ is the mound height profile which defines the vertical height of the mound for an adiabatic gas expressed in flux coordinate (ψ) instead of r . The values of ρ , p and their derivatives become zero smoothly at $z = Z_0(\psi)$.

Putting equation (7) in equation (4) we obtain the Grad-Shafranov equation (hereafter GS) for an adiabatic gas.

$$\frac{\Delta^2 \psi}{4\pi r^2} = -\rho g \frac{dZ_0}{d\psi}. \quad (8)$$

The GS equation is a coupled non-linear elliptic partial differential equation. We have solved the GS equation numerically following the algorithm outlined in Appendix A.

3 RESULTS AND ANALYSIS OF SOLUTIONS OF THE GS EQUATION

We have made several runs with different mound height profiles. The solutions show expected behaviour of matter pushing field lines outwards until the tension in the field lines supports the gas pressure. The deformation of the field lines increases with larger base pressure and density of the mound until the solution breaks down after a threshold density (see Section 3.3). In this section we discuss the solutions from some sample runs and the range of parameters for which equilibrium solutions can be found.

3.1 Modelling the magnetically supported accretion mound

We will assume a hydrogen-poor plasma ($\mu_e = 2$) being confined in the mound (Brown & Bildsten 1998). We restrict the analysis to the gaseous state before ions form a liquid phase. The electrostatic coupling parameter (Γ) gives a rough estimate whether matter is solid ($\Gamma \gg 1$), liquid ($\Gamma \simeq 1$) or gas ($\Gamma < 1$) (e.g. Litwin et al. 2001)

$$\Gamma = \frac{Z^2 e^2}{k_B T} \left(\frac{4\pi n}{3} \right)^{1/3} \simeq 1.1 \left(\frac{Z^2}{A^{1/3}} \right) \left(\frac{\rho}{10^8 \text{ g cm}^{-3}} \right)^{1/3} \left(\frac{10^8 \text{ K}}{T} \right). \quad (9)$$

Hence, mounds of base densities $< 10^8 \text{ g cm}^{-3}$ are considered for this work. To determine the appropriate form of an equation of state, we first check if the plasma is non-relativistic ($\gamma = 5/3$) or relativistic ($\gamma = 4/3$) by evaluating the adiabatic index ($\gamma = d \ln p / d \ln \rho$) from the expression of the fermionic pressure for degenerate electron gas (Chandrasekhar 1967). As shown in Fig. 1, at $\rho \simeq 10^7 \text{ g cm}^{-3}$, we have $\gamma \geq 1.4$. For densities lower than this, γ rises and reaches 1.667 asymptotically. Since, for $\rho \leq 10^7 \text{ g cm}^{-3}$, γ is significantly higher than 1.33, we model the accreted matter in the mound as a degenerate non-relativistic electron gas with a thermal proton background whose pressure is negligible compared to the electron

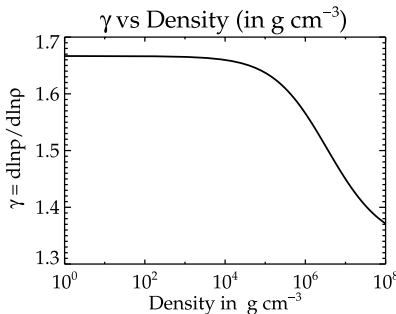


Figure 1. Plot of adiabatic index (γ) versus density (g cm^{-3}). For lower densities, γ asymptotically converges to 1.667, which is the value obtained in the non-relativistic approximation. For $\rho \geq 10^8 \text{ g cm}^{-3}$, γ converges to 1.333, which is the value obtained in the ultra-relativistic approximation.

degeneracy pressure. The equation of state for such a system is (values quoted are in cgs)

$$p = \left[(3\pi^2)^{2/3} \frac{\hbar^2}{5m_e} \right] \left(\frac{\rho}{\mu_e m_p} \right)^{5/3} = 3.122 \times 10^{12} \rho^{5/3}. \quad (10)$$

The plasma is dominated by degeneracy pressure if $(T/T_F) < 1$, where T_F is the Fermi temperature:

$$T_F = \frac{m_e c^2}{K_B} \left(\sqrt{X_F^2 + 1} - 1 \right),$$

$X_F = p_F / m_e c = (1/m_e c) [(3\hbar^3)/(8\pi\mu_e m_p)]^{1/3} \rho^{1/3}$, p_F being the Fermi momentum. Observed X-ray continuum from high-mass X-ray binaries (Coburn et al. 2002; Becker & Wolff 2007) indicate that photospheric temperatures in the hotspot are in the range of $T \sim 5\text{--}10 \text{ keV}$. The Fermi temperature falls below 10 keV only for a thin layer [$\sim 0.01 Z_0(\psi)$, from equation 7] at the top and a major fraction of the mound has a Fermi temperature larger than 100 keV. Comparison to the temperature profiles obtained including heat transfer effects by Brown & Bildsten (1998) shows that the temperature inside the mound remains lower than Fermi temperature at greater depths. Thus, modelling the confined accreted matter as a degenerate mound is appropriate.

We have solved the GS equation for different forms of the mound height profile (e.g. Hameury et al. 1983; Litwin et al. 2001)

$$Z_0(\psi) = Z_c \left[1 - \left(\frac{\psi}{\psi_p} \right)^2 \right], \quad (11)$$

$$Z_0(\psi) = Z_c \exp \left[-2 \frac{\psi}{\psi_p} \right], \quad (12)$$

$$Z_0(\psi) = Z_c \left[1 - \left(\frac{\psi}{\psi_p} \right)^4 \right]. \quad (13)$$

The mound height profile depends on the mass-loading function at the accretion disc and redistribution of matter in the shock region for which at present there is no clear knowledge. We resort to evaluating the density by specifying the mound height as a simple function of ψ , subject to the constraint $\rho \rightarrow 0$ as $r \rightarrow R_p$, so that the mound is confined within the polar cap. In most of the analysis, we have used equation (11), which has relatively shallow gradients and helps in speeding up the numerical convergence.

3.2 Solutions from the GS solver

We discuss here results from two sample runs.

Case (a): $Z_c = 55 \text{ m}$

case (b): $Z_c = 70 \text{ m}$,

with the mound height profile specified by equation (11) and the magnetic field $B = 10^{12} \text{ G}$. The value Z_c was chosen to keep maximum base densities less than 10^8 g cm^{-3} (as discussed in Section 3.1).

For case (a), the total mass of the mound is $\sim 9 \times 10^{-13} M_\odot$ and maximum base density is $\sim 4.7 \times 10^7 \text{ g cm}^{-3}$. For case (b), the total mass of the mound is $\sim 2.13 \times 10^{-12} M_\odot$ and maximum base density is $\sim 6.8 \times 10^7 \text{ g cm}^{-3}$. The mound is in the shape of a flat thin layer on the surface of the star, confined within the polar cap (Fig. 2). Contours of ψ from the solution, which represent the magnetic field lines (as $\mathbf{B} \cdot \nabla \psi = 0$), are plotted in Fig. 3. From the figure, we see that the field lines are bent to support the pressure of the confined matter. The distortion is more in case (b). Field lines are pushed outwards from the initial configuration resulting in bunching of field lines and increase in the field strength.

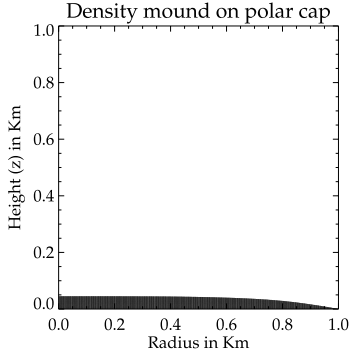


Figure 2. The shape of the accretion mound plotted along the r and z axes in equal scale to show the real aspect ratio. The mound is like a thin flat layer on the pole.

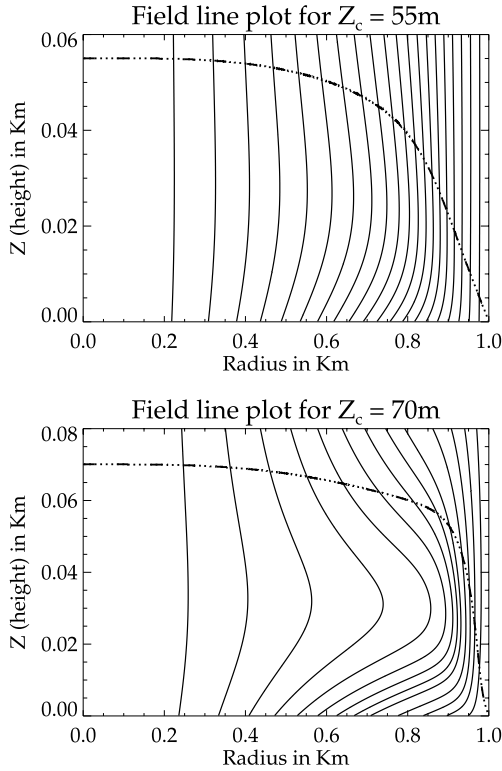


Figure 3. Solution for $Z_c = 55$ m (top) and 70 m (bottom), cases (a) and (b) in the text, respectively. Solid lines are field lines from the GS solution. The dash-dotted line represents the top of the mound.

3.3 Valid parameter space for existence of solution

Hameury et al. (1983) mention in their work that for the configuration of mound height profiles they had considered, no solution was found for a field lower than a critical value. We observe the same for different values of the magnetic field and different mound height profiles. For a fixed magnetic field, we find that for the parabolic profile (equation 11), a stable solution exists for only up to a maximum threshold mound height (Z_{\max}). For mounds higher than this, the ψ function keeps oscillating between multiple states with closed magnetic loops during the iteration process and convergence to a unique solution is not reached. For a magnetic field of $\sim 10^{12}$ G, the maximum height of a mound for a stable solution was found to be $Z_{\max} \sim 70$ m. For a mound higher than this threshold, $Z_c = 75$ m, the mean ψ is seen to oscillate between two states (Fig. 4).

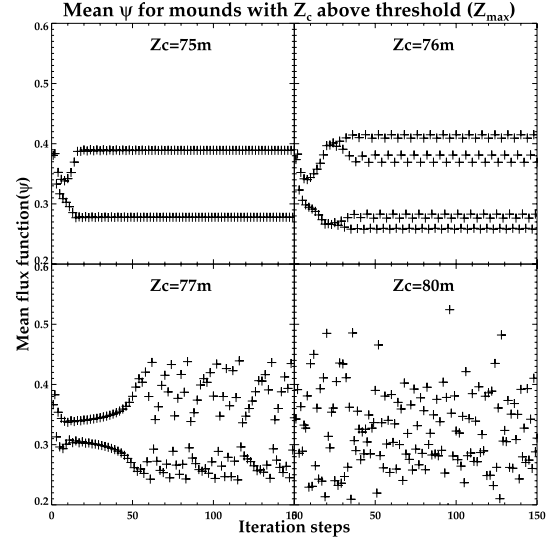


Figure 4. Mean ψ as a function of iteration steps for different mound heights above the stability threshold. The mean ψ is seen to oscillate between multiple states. Beyond a certain Z_c it passes through different states randomly.

The configuration of these two states is similar in nature to those displayed in Fig. 5. For higher mounds, the branches of the mean ψ bifurcate to multiple states similar to a pitchfork diagram. The formation of closed magnetic loops, also reported in Hameury et al. (1983), PM04 and Payne & Melatos (2007), appears to indicate loss of equilibria. We have tried different simulations to check for the existence of solutions beyond the threshold, e.g. higher resolution runs or improving the initial guess solution by starting from a previously converged solution or increasing the radial extent of the grid. However, stable solutions were not found for heights greater than the threshold Z_{\max} .

Fig. 6 shows the maximum values of Z_{\max} (equation 11) for a given field up to which solutions exist. The maximum allowed height (Z_{\max}) has a power-law dependence on B :

$$\log_{10}(Z_{\max}) = -3.676 + 0.461 \log_{10}(B), \quad (14)$$

where Z_{\max} is in metres and B is in Gauss. A similar magnetic field to Z_{\max} scaling was observed for the solution with different mound height profiles; e.g. for equation (12) we get $\log_{10}(Z_{\max}) = -3.79 + 0.46 \log_{10}(B)$ and for equation (13) we get $\log_{10}(Z_{\max}) = -3.61 + 0.45 \log_{10}(B)$, which indicates that this is a generic feature of the GS equation in the current set-up.

Such a scaling relation can be understood approximately by comparing the variation of the pressure and the magnetic field over

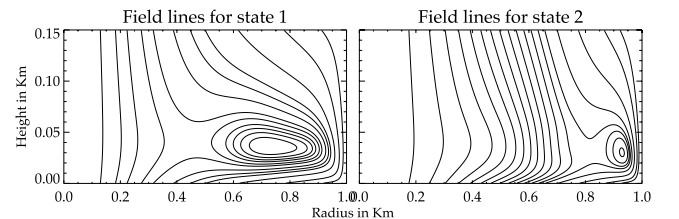


Figure 5. The ψ function at two intermediate iteration steps (79th and 80th) of the GS solver for a mound of height 75 m. Closed magnetic loops are seen to form which indicate loss of equilibria. At different iteration steps, ψ passes through states similar to states 1 and 2 depicted here without reaching convergence.

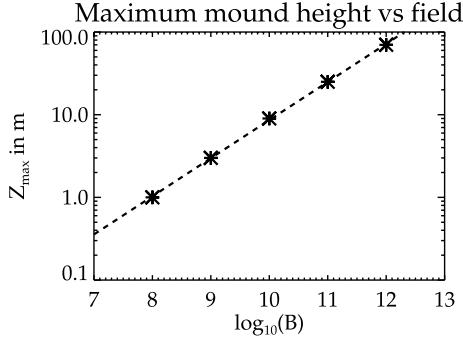


Figure 6. Maximum height of the mound (Z_{\max}) that can be supported by different surface field strengths. The mound height profile of equation (11) is assumed. The dashed line shows a power-law fit to the points. Valid solutions can be obtained only for parameters below the line, above which the GS code does not converge.

different length-scales which balance each other. Lateral variation in pressure over a scale R_p is balanced by tension from the curvature in a magnetic field which occurs over a length-scale Z_{\max} . Hence, from equations (7), (10) and (11), we get

$$\left. \begin{aligned} \rho &\sim AZ_{\max}^{3/2}, \quad p \propto Z_{\max}^{5/2}, \\ \nabla p &\simeq \mathbf{B} \cdot \nabla \mathbf{B} \rightarrow \frac{p}{R_p} \simeq \frac{B^2}{Z_{\max}}, \\ Z_{\max} &\propto B^{4/7}. \end{aligned} \right\} \quad (15)$$

Litwin et al. (2001) have shown that ballooning instability will disrupt the equilibria if $\Delta b > 7.8R_p/[(\gamma - 1)Z_0(\psi)]$, where β is the ratio of plasma pressure to magnetic pressure [$p/(B^2/8\pi)$]. Using $p \sim k_{\text{ad}}\rho^{5/3}$ (equation 10) and $\rho \sim AZ_{\max}^{3/2}$ (equation 7), we can write the stability criterion obtained by Litwin et al. (2001) as

$$\log_{10}(Z_{\max}) > -5.1 + \frac{4}{7}\log_{10}B, \quad (16)$$

which is very close to the observed dependence of Z_{\max} and B as obtained from our numerical solutions. Thus, the limit represented by equation (14) may result from ballooning-type pressure-driven instabilities where the curvature of the magnetic field can no longer support the plasma pressure (equations 15 and 16) and the equilibrium solution cannot be obtained. Hence, for our analysis of the cyclotron line features in the following section, we restrict ourselves to mounds of height less than 70 m for a dipole field of 10^{12} G. A detailed study of the stability analysis of our solutions will be reported in a future publication (Mukherjee, Bhattacharya & Mignone, in preparation).

4 CYCLOTRON RESONANCE SCATTERING FEATURES

The major part of the mound forms an optically thick medium with cyclotron line formation taking place in a thin layer located at the top surface. The depth of the line-forming region may be estimated as $l \sim Z_0 - z$, where Z_0 (the mound height profile) is the top height of the mound at a given r . From the definition of optical depth and using equation (7) for the density distribution, we find the relation between the optical depth and thickness of the line-forming region as

$$\tau = \frac{A\sigma}{\mu_e m_p} l^{5/2}, \quad (17)$$

where m_p is proton mass and σ is the scattering cross-section. For Thomson scattering ($\sigma = \sigma_{\text{Th}}$), $\tau \simeq 1$ occurs at a depth of

~ 1.1 mm, and for cyclotron resonance scattering ($\sigma \sim 10^5 \sigma_{\text{Th}}$), $\tau \simeq 1$ occurs at $11.3 \mu\text{m}$. Thus, cyclotron line formation takes place in a thin layer at the top of the mound. Variation in the local magnetic field at the top of the mound is expected to cause variation in the cyclotron spectra. Modelling of the CRSFs taking into account the contribution of different parts of the mound to the LOS is presented in the following section.

4.1 Modelling cyclotron spectra

The emission profile from a point on the mound depends on the strength and direction of the magnetic field and the angle between the emergent radiation and the local normal to the mound surface, which vary with position due to curvature of the field lines and the shape of the mound surface, respectively. We divide the mound into small area elements [$\Delta A_{r_i, \theta_j}$ in a (r, θ) grid in cylindrical coordinates on the polar cap] and find the local magnetic field vector and local normal to the mound for each element, assuming them to be constant over the area element. The resultant cyclotron spectrum is constructed by integrating the weighted contribution of emission from all parts of the mound towards an LOS

$$F = \sum_{i,j} I(\theta_{\alpha i}) \Delta A_{r_i, \theta_j} \cos \theta_{\alpha i}, \quad (18)$$

where I is the normalized intensity at the mound surface and the angle $\theta_{\alpha i}$ (equation B6) is the angle between the direction of emission at the mound surface and the local normal to the surface. For integrating the intensity over the mound, we have chosen a radial grid with resolution equal to or higher than the resolution in the radial direction of the GS solution.

The cyclotron line energy is given by

$$E_n = n E_{c0} \sqrt{1-u} \left(1 - \frac{n}{2} \left(\frac{E_{c0}}{511 \text{ keV}} \right) \sin^2 \theta_{\alpha b} \right), \quad (19)$$

where $n = 1, 2, 3, \dots$, is the order of the harmonic, $E_{c0} = 11.6 B_{12}$ in keV, $\theta_{\alpha b}$ is the angle between the direction of emission and the local magnetic field (equation B5) and $u = r_s/r$, r_s being the Schwarzschild radius. The factor $\sqrt{1-u}$ gives the gravitational redshift of the line.

Equation (19) is correct to second order in the small parameter $E_{c0}/(511 \text{ keV})$, and is adequate for the field strengths we consider in this work. In our studies, we consider only the effect of the fundamental $n = 1$ line. The accurate dependence of the width and depth of the CRSF on the angle $\theta_{\alpha b}$ can be obtained by solving radiative transfer equations in the mound. This is beyond the scope of the present work and will be addressed in a future publication (Kumar et al., in preparation). For our present work, we model the cyclotron feature by a Gaussian profile with line centres from equation (19) and model the dependence on the angle $\theta_{\alpha b}$ of the line width $\Delta E/E_c$ and the relative depth by interpolating from the results presented in Schönherr et al. (2007) for the slab 1-0 geometry.

We incorporate effects of gravitational light bending (equation B1) following the approximate formula given by Beloborodov (2002). For the intrinsic intensity profile, we use a form $I(\theta_{\alpha i}) = I_0 + I_1 \cos \theta_{\alpha i}$, but set $I_1 = 0$ for most of our analysis. To simulate the finite energy resolution of the detectors, we convolve the spectra with a normalized Gaussian with the standard deviation of a fraction f of the local energy

$$W(E, E') = \frac{1}{\sqrt{2\pi}\sigma} \exp \left(\frac{-(E - E')^2}{2\sigma^2} \right), \quad \sigma \sim f E'. \quad (20)$$

Detectors currently used for observations in X-ray astronomy usually have an energy resolution of 10–20 per cent ($f \simeq 0.1$ – 0.2). We carry out the above analysis at different phases of rotation of the neutron star to perform a phase-dependent study of the spectra. The nature of the spectra also depends on the relative orientation of the mound (inclination angle η_p) and the LOS (angle i) with respect to the spin axis of the neutron star, which are treated as free parameters (see Appendix B for details on the geometry).

4.2 Results: cyclotron spectra from a single mound

We have carried out simulation runs for the cyclotron spectra using the solutions of the magnetic field obtained from the GS solver. For most of our analysis in this section, we use the solution with profile equation (11). Although the shape and nature of the CRSF will change for different profile functions, we can draw some general conclusions about the dependence of the cyclotron spectra on the local magnetic field.

We first consider the case of emission from a single hotspot at one of the poles. Fig. 7 shows the light curve from a mound of height $Z_c = 45$ m at a pole with inclination $\eta_p = 10^\circ$ and LOS $i = 30^\circ$ (see Appendix B for definitions of i and η_p). The inset plots show the cyclotron spectra convolved with a Gaussian with $f = 0.1$ (equation 20), at two rotation phases 32° and 200° . Although the magnitude of the field at the top of the mound varies by ~ 27 per cent in this case (Fig. 8), the line centre of the CRSF shows less than 0.2 per cent change about a mean of ~ 9.6 keV. As the continuum emission is assumed to be isotropic and uniform, and also since gravitational bending redirects the light rays in directions well away from straight trajectories, all parts of the mound contribute towards a given LOS at all phases. This gives a resultant averaged spectrum with a very little phase dependence of the CRSF from a single pole.

For mounds with a large distortion of the surface magnetic field (e.g. for $Z_c = 70$ m), the field at the edge rises to ~ 4.6 times the original dipole value (see Fig. 8). We find two distinct CRSF fundamentals at two distinct energies (Fig. 9). The feature at a lower energy, for a field of $\sim 10^{12}$ G, originates near the centre of the mound while that at a higher energy arises in the high field regions near the periphery of the mound (Fig. 8). We emphasize that this multiple-featured spectrum is a result of the variation of the local field strength and does not represent multiple harmonics,

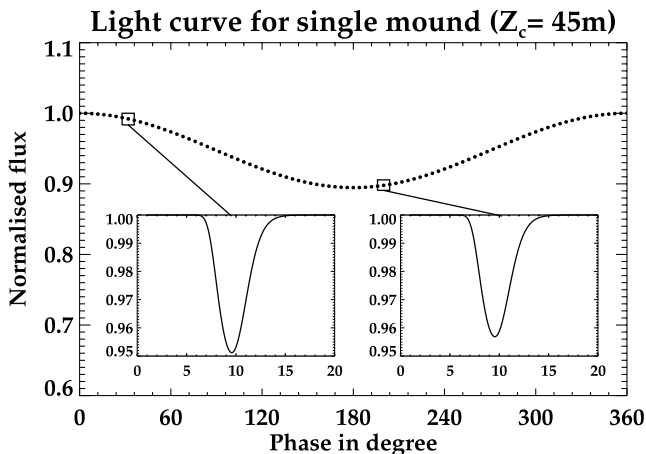


Figure 7. The light curve of one-pole mound for $Z_c = 45$ m, $\eta_p = 10^\circ$ and $i = 30^\circ$ (Appendix B). Insets show the spectra at the two rotation phases marked. No significant variation of the line energy is seen. A detector resolution of 10 per cent was assumed (equation 20).

Variation of B at the top of the mound

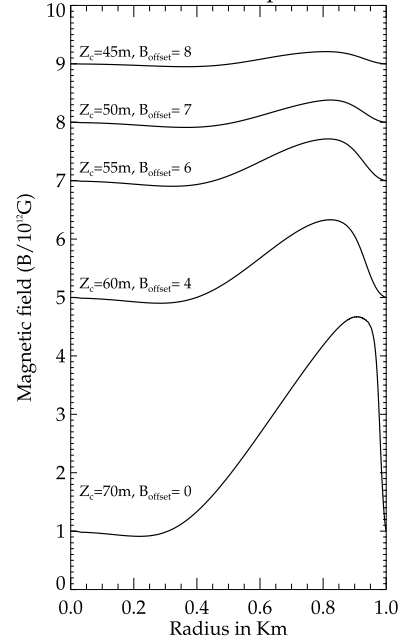


Figure 8. The variation of the strength of the magnetic field with radial distance at the top of the mound, for different Z_c . The plots are offset by an amount (B_{offset}) for clarity. The maximum magnetic field at the top is several times the surface dipole field due to a distortion from the pressure of the accreted matter.

Spectra from different mounds

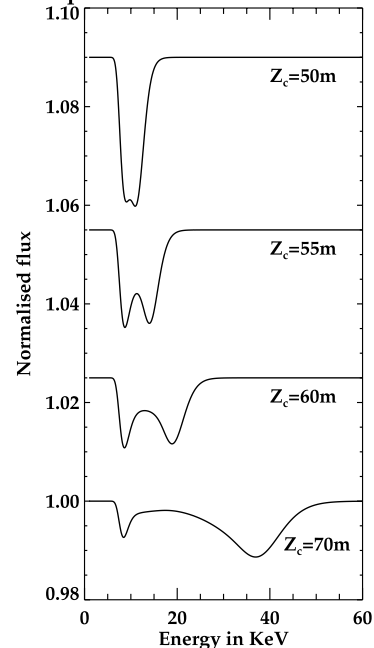


Figure 9. CRSFs from mounds of different heights. The spectrum for each mound shows two CRSF fundamentals at two distinct energies, corresponding to the undistorted dipolar field and the region with a large distortion of the magnetic field, respectively (see Fig. 8).

as only $n = 1$ features have been included in our computation. The energy ratio of these features may therefore be arbitrary and not follow a harmonic relation.

The line centres of the individual peaks show little variation with phase but the relative depth of the peaks depends on the viewing

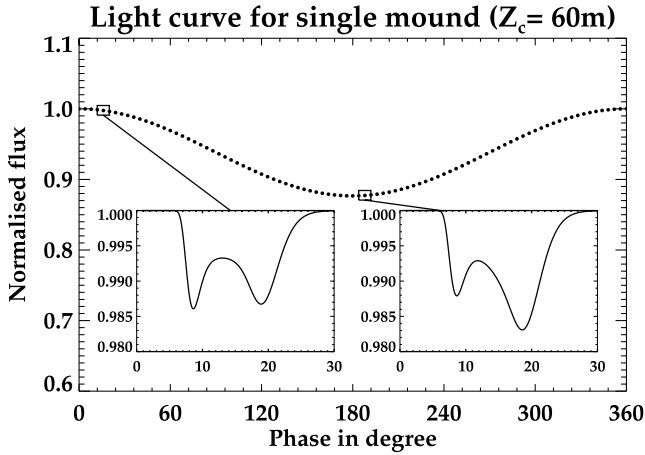


Figure 10. The light curve of one-pole mound with $Z_c \sim 60$ m, $\eta_p = 10^\circ$ and $i = 30^\circ$ (Appendix B). Insets show the spectra at two rotation phases marked. Multiple CRSFs are seen with variation of the relative depth with phase, but no phase dependence of the line energies. A detector resolution of 10 per cent was assumed (equation 20).

geometry and the phase angle. Fig. 10 shows the light curve and spectra (with $f = 0.1$ in equation 20) from a mound of $Z_c \sim 60$ m with $\eta_p = 10^\circ$ and $i = 35^\circ$, where the relative depth of the CRSF varies with phase. The degree of their variation depends on the relative orientation of the pole and the LOS, occurring for a certain range of viewing angles ($25^\circ \leq i \leq 40^\circ$ for a pole at $\eta_p = 10^\circ$ in the present case). Two distinct CRSFs are observed for all mounds of an appreciable magnetic field distortion at the top and all viewing geometries, which shows that it is a generic feature of the cyclotron lines originating from the mound.

The cyclotron features are dominated by the field structures near the periphery of the mound as these regions have a larger emitting area. For GS solutions with a mound height profile as in equation (11), the regions of the higher magnetic field distortion occur near the edge of the polar cap. Hence, we observe two CRSFs of comparable depths for all mounds with profile equation (11). However, if we use an exponential profile (equation 12) which falls off sharply with r , regions of a larger field distortion occur much closer to the axis (Fig. 11), and the CRSF is dominated by the undistorted field in the outer region. A shallow feature at ~ 18 keV is contributed by the higher field regions nearer to the axis. This shows that the CRSF is heavily influenced by the geometry and distribution of the local field as well as the structure of the mound.

4.3 Effects of finite energy resolution of detectors

The finite energy resolution of the detector can make the two absorption features indistinguishable if closely placed. In Fig. 12 we show the effect of the Gaussian convolution with different values of f (equation 20). For $f = 0.2$, the two peaks are indistinguishable. For mounds of a lower height (e.g. $Z_c = 45$ m), the two CRSFs become indistinguishable at a much smaller f . Thus, the finite energy resolution of the detector can often mask the effects of the internal magnetic field structure on the CRSF. However, for mounds of a higher height, the two CRSFs have centres far enough to be distinguishable even with $f = 0.2$.

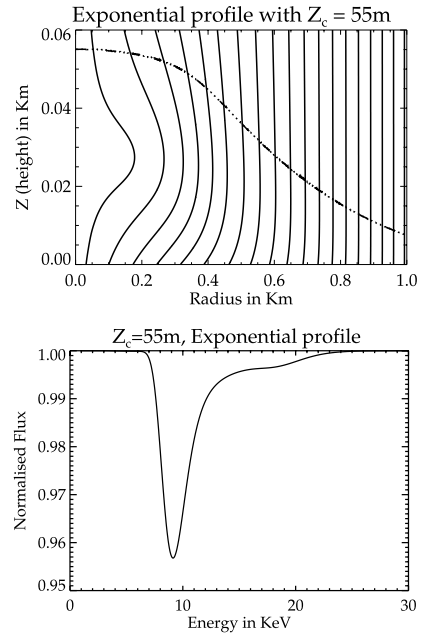


Figure 11. Magnetic field line structure (upper panel) for a mound with $Z_c \sim 55$ m with an exponential mound height profile equation (12) and the spectrum emitted (lower panel). The spectrum is dominated by area elements near the polar cap edge (corresponding to the region of the undistorted field in this case) as they span larger areas. The shallow feature at ~ 18 keV corresponds to the region of a large field distortion closer to the axis.

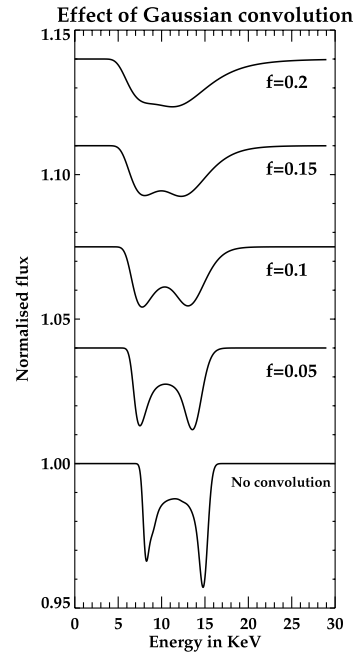


Figure 12. The effect of the finite detector resolution modelled by convolving the spectra with a Gaussian function. Results for different values of f (equation 20) are shown. The double-CRSF nature of the spectra disappears for $f \geq 0.2$, corresponding to a 20 per cent energy resolution of the detector.

4.4 Emission from two anti-podal poles

Many systems show a variation in the cyclotron energy with the phase of rotation of the neutron star, e.g. $\Delta E_{\text{cyc}}/E_{\text{cyc}} \sim 10$ per cent for Vela X-1 (Kreykenbohm et al. 2002), ~ 20 per cent for 4U0115+63 (Heindl et al. 2004; Baushev 2009), ~ 25 per cent

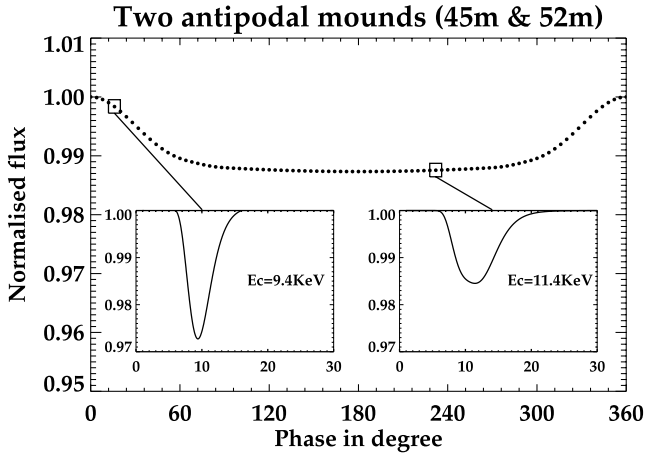


Figure 13. The light curve for two anti-podal mounds, $Z_c \sim 45 \text{ m}$ and 52 m , with $\eta_p = 30^\circ$ and 150° respectively, and $i = 30^\circ$ (Appendix B). Insets show the spectra at the two rotation phases marked. The CRSF shows a 20 per cent change in line energy with phase. A detector resolution of 15 per cent was assumed (equation 20).

for Her X-1 (Klochkov et al. 2008a), GX 301-2 (Kreykenbohm et al. 2004) and ~ 30 per cent for Cen X-3 (Burderi et al. 2000; Suchy et al. 2008). From our simulations of CRSFs for emission from a single hotspot, we find very little variation of the line energy with the rotation phase. However, if emission is considered from two antipodal hotspots at opposite poles with a slight difference in the mound height due to asymmetric accretion, then the line centre of the resultant CRSF shows a stronger phase dependence. Fig. 13 shows the light curve for a neutron star with two anti-podal poles at $\eta_p \sim 30^\circ$ and 150° , having mounds of height $Z_c \sim 45 \text{ m}$ and 52 m , respectively, and an observer at inclination $i = 80^\circ$. The simulation is carried out by assuming a uniform and isotropic continuum intensity normalized to 1 at both poles, which may not be valid in reality due to difference in accretion rates at the two poles. However, for small differences in the mound heights considered here, we ignore the differential luminosity effect and draw some general conclusions about the behaviour of the cyclotron line energies. The spectra are convolved with a Gaussian function with $f = 0.15$ (equation 20).

The light curve is not sinusoidal unlike the case of a single pole (Figs 7 and 10). The line energy of the CRSF varies by $\Delta E_c \sim 20$ per cent over a full rotation cycle. The spectrum from the pole nearer to the LOS dominates the CRSF. The observed variation in the line energy of course depends on the viewing geometry defined by the angles i and η_p . A proper evaluation of the spectra for a two-pole case would require the knowledge of the accretion rate and local temperature of the hotspots, but it may be concluded that in the presence of multiple hotspots, the CRSF line energy will show a significant phase dependence.

5 DISCUSSION AND CONCLUSIONS

We have modelled the structure of the accretion mound by solving for the static magnetic equilibria described by the GS equation. For mounds of a total accreted mass of $\sim 10^{-12} M_\odot$ (Section 3.2), there is an appreciable distortion of the magnetic field. We have found that for a given surface field strength, stable solutions to the GS equation are not found for mounds of height higher than a threshold (Section 3.3). Beyond the threshold, field lines with closed loop configurations are formed, and may indicate the onset of pressure-

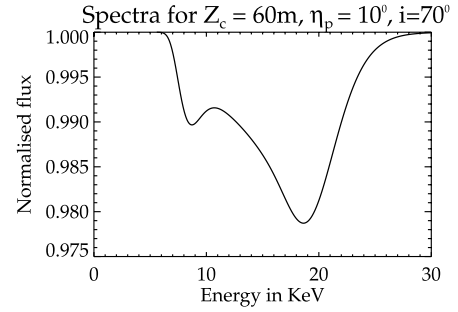


Figure 14. The CRSF from a mound of height $Z_c = 60 \text{ m}$ with mound height profile equation 11, $\eta_p = 10^\circ$ and $i = 70^\circ$ (see Appendix B). The undistorted field produces the small feature at $\sim 8 \text{ keV}$. The distorted field near the polar cap edge is the dominant contributor to the CRSF, producing a dip at $\sim 18 \text{ keV}$. This shows that the field inferred from the CRSF line energy may not depict the surface dipole field, but the field distorted due to accreted matter.

driven MHD instabilities. Therefore, we restrict our analysis to mound heights for which equilibrium solution is obtained.

Using the mound structure obtained from the GS equation, we have simulated the cyclotron spectra which will originate from its mound surface. We have integrated the emission from different parts of the mound to find the resultant spectra and have performed a phase-dependent study of the spectra. We have assumed a Gaussian model for the CRSF fundamental and have incorporated effects of the gravitational bending of the light and finite energy resolution of the X-ray detectors (Section 4.1). From our analysis of the phase-dependent spectra (Sections 4.2–4.4) we can draw some general conclusions.

(i) *CRSFs need not represent the dipole field.* The CRSFs are heavily influenced by the distortion of the local field caused by the pressure of the confined accreted matter. The line energy of the CRSFs may not always represent the intrinsic dipole magnetic field. As shown in Fig. 14, the small dip at $\sim 8 \text{ keV}$ is the redshifted cyclotron feature due to the surface field of 10^{12} G , which may not be observed in practice in the presence of noise and poor detector resolution. The CRSFs at $\sim 18 \text{ keV}$ resulting from the distorted field will be the dominant feature in the spectrum. For mounds of height $Z_c \sim 70 \text{ m}$, the maximum distortion in the field can be as large as 4.6 times the dipole value.

(ii) *Multiple, anharmonic CRSFs.* From our simulations we observe multiple CRSF fundamentals from a single mound with a considerable field distortion (see Figs 9 and 10). A real spectrum will also contain multiple CRSF harmonics which will add to the complexity of the spectrum. Several high mass x-ray binaries (HMXBs) show multiple CRSF where the line centres have anharmonic separation, e.g. $E_c \sim 22$ and 47 keV for 4U 1538–52 (Rodes-Roca et al. 2009), ~ 23 and 51 keV for Vela X-1 (Kreykenbohm et al. 2002), ~ 45 and 100 keV for A 0535+26 (Kendziorra et al. 1994; Caballero et al. 2007), ~ 26 , 49 and 74 keV for V0332+53 (Makishima et al. 1990; Pottschmidt et al. 2005) and ~ 36 and 63 keV for EXO 2030+375 (Reig & Coe 1999; Klochkov et al. 2008b). More details on the properties of these sources can be found in the reviews by Mihara et al. (2007) and Lutovinov & Tsygankov (2008).

Anharmonic line spacing due to an intrinsic non-dipolar field has been discussed by Nishimura (2005). Our results show that a strong non-dipolar structure can be generated in the accretion process itself.

(iii) *Effect of detector resolution.* The detectability of multiple cyclotron features depends on the energy resolution of the detector. For detectors with a poor energy resolution, the multiple fundamental features will be masked as shown in Fig. 12. However, for mounds with a large field distortion ($Z_c \sim 60$ – 70 m), multiple absorption features will still be observed with detectors that have an energy resolution of ≤ 20 per cent.

(iv) *CRSF phase dependence – one pole.* We find no appreciable spin phase dependence of the line energy of a given CRSF from a single mound (Fig. 7) despite there being a considerable local variation of the magnetic field. This may be attributed to the fact that all parts of the mound contribute towards a given LOS at any phase due to effects of gravitational light bending and assumption of isotropic local emission. However, we find that the relative depth of the multiple CRSF depends on phase and viewing geometry as shown in Fig. 10.

(v) *CRSF phase dependence – two poles.* Line energy variation is however observed if emission from both poles with slightly different mound heights is considered (Section 4.4). For emission from two anti-podal mounds of height $Z_c \sim 45$ and 52 m, the CRSF line energy varies by 20 per cent during one spin cycle, similar to what is observed for many sources. Thus, we conclude that emission from multiple accretion mounds will result in a strong variation of the line energy of the CRSF with spin phase.

(vi) *Dependence on mound structure.* CRSFs are dominated by field structure at the mound periphery due to the larger physical area of this region. Different structure and density distribution of the mound would cause different distributions of the local field. Figs 9 and 11 show the difference in the CRSF from a mound of the same maximum height ($Z_c = 55$ m) but different mound height profiles. The strong dependence of the spectra on the structure and size of the mound suggests that with variation in the accretion rate, the observed line profiles and energies may change, contributing to a luminosity dependence of the spectrum.

Some sources such as Her X-1 (Staubert et al. 2007) and A 0535+26 (Klochkov et al. 2011) show a positive correlation between luminosity and line energy. In our picture, this can be attributed to the presence of a strong non-dipolar component in the field due to an increase in the mass of the mound resulting from an increase in the accretion rate. Our simulations show that for a small change of mound size, we have an appreciable change in the maximum magnetic field at the top of the mound (Fig. 8), e.g. between Z_c of 55 and 60 m, the maximum field at the top of the mound changes by ~ 36 per cent. Since we work in the static limit and do not consider accretion rate as a parameter in our simulations, we cannot directly probe the luminosity dependence of the spectrum. However, we can conclude that small changes in the height of the mound can result in significant changes in the magnetic field inferred from the CRSF.

(vii) *Effect of anisotropic continuum.* We have also carried out runs with mildly anisotropic continuum intensity profiles, $I(\theta_{al}) = I_0(1 + \cos \theta_{al})$, and have found no appreciable phase dependence of the line energy of a one-pole CRSF although the percentage modulation of the flux was larger. However, if continuum is highly anisotropic, e.g. $I = [\sin 2\theta_{al}/(2\theta_{al})]^2$, then the resultant spectra are found to be phase dependent. However, such strong beaming may not be realistic in the context of HMXB pulsars.

(viii) *Screening effect from overlying column.* Effects of the partial screening of the mound by an atmosphere of accreted matter have not been considered in our simulations. An optically thick blanket of the settling plasma can screen a fraction of the mound depending on the viewing geometry. The effect of screening can

be estimated approximately by using the velocity profile of the settling flow from Becker & Wolff (2007): $v(z) = 0.49c\sqrt{z/R_p}$, for a neutron star of mass $\sim 1.4 M_\odot$ and radius ~ 10 km, mean plasma temperature ~ 10 keV and magnetic field $\sim 10^{12}$ G. For an accretion rate of $\dot{M} \sim 10^{16}$ g s $^{-1}$ and a mound of height $Z_c \sim 70$ m (maximum allowed Z_c for equation 11), we get the Thomson optical depth as $\tau \sim 1.57 \times 10^{-5} \ell$, where ℓ is the line element along the LOS through the accretion column. For a hotspot of radius $R_p \sim 10^5$ cm, we see that regions near the axis will be optically thick along a radial line from the axis (in local cylindrical geometry of the mound). The degree of screening of different parts of the mound will vary with spin phase, resulting in phase-dependent spectra.

Thus, we conclude from this work that the distortions in the local magnetic field due to the confinement of accreted matter at the polar cap have a considerable influence on the phase-resolved spectra from accreting binary neutron star systems. Current observations often have poor count statistics and involve averaging in phase due to which many of the details in the spectra may be lost. Future missions like *ASTROSAT* (Agrawal et al. 2005; Koteswara Rao et al. 2009) with higher sensitivity and better energy resolution can help us analyse the spectra in greater detail and provide us clues to the nature, shape and geometry of the accretion mound. A more detailed analysis including dynamic simulations of the emitting region and full radiative transfer would help us investigate effects such as line-energy–luminosity correlation, anharmonic separation of the CRSF energies and asymmetric shape of the CRSF.

ACKNOWLEDGMENTS

We thank CSIR India for Junior Research fellow grant, award no. 09/545(0034)/2009-EMR-I. We are very thankful to Andrea Mignone for his help and suggestions in setting up simulation runs with *PLUTO*. We thank Dr Kandaswamy Subramanian, Dr Ranjeev Misra and Sandeep Kumar from IUCAA for useful discussions and suggestions during the work, and IUCAA HPC team for their help in using the IUCAA HPC, where most of the numerical computations were carried out. We would also like to thank Dr Rüdiger Staubert for his suggestions in improving the text and the anonymous referee for his valuable suggestions and comments.

REFERENCES

- Agrawal P. C., The Astrosat Collaboration, 2005, *Bull. Astron. Soc. Ind.*, 33, 351
- Araya R. A., Harding A. K., 1999, *ApJ*, 517, 334
- Araya-Góchez R. A., Harding A. K., 2000, *ApJ*, 544, 1067
- Baushev A. N., 2009, *Astron. Rep.*, 53, 67
- Becker P. A., Wolff M. T., 2007, *ApJ*, 654, 435
- Beloborodov A. M., 2002, *ApJ*, 566, L85
- Bhattacharya D., van den Heuvel E. P. J., 1991, *Phys. Rep.*, 203, 1
- Biskamp D., 1993, *Nonlinear Magnetohydrodynamics*. Cambridge Univ. Press, Cambridge
- Brown E. F., Bildsten L., 1998, *ApJ*, 496, 915
- Burderi L., Di Salvo T., Robba N. R., La Barbera A., Guainazzi M., 2000, *ApJ*, 530, 429
- Caballero I. et al., 2007, *A&A*, 465, L21
- Chandrasekhar S., 1967, *An Introduction to the Study of Stellar Structure*. Dover, New York
- Coburn W., Heindl W. A., Rothschild R. E., Gruber D. E., Kreykenbohm I., Wilms J., Kretschmar P., Staubert R., 2002, *ApJ*, 580, 394
- Cumming A., Zweibel E., Bildsten L., 2001, *ApJ*, 557, 958
- Ghosh P., Lamb F., 1978, *ApJ*, 223, L83
- Ghosh P., Pethick C. J., Lamb F. K., 1977, *ApJ*, 217, 578

- Hameury J. M., Bonazzola S., Heyvaerts J., Lasota J. P., 1983, *A&A*, 128, 369
- Harding A. K., Preece R., 1987, *ApJ*, 319, 939
- Heindl W. A., Rothschild R. E., Coburn W., Staubert R., Wilms J., Kreykenbohm I., Kretschmar P., 2004, in Kaaret P., Lamb F. K., Swank J. H., eds, *AIP Conf. Ser. Vol. 714, X-Ray Timing 2003: Rossi and Beyond*. AIP, New York, p. 323
- Kendziorra E. et al., 1994, *A&A*, 291, L31
- Klochkov D. et al., 2008a, *A&A*, 482, 907
- Klochkov D., Santangelo A., Staubert R., Ferrigno C., 2008b, *A&A*, 491, 833
- Klochkov D., Staubert R., Santangelo A., Rothschild R. E., Ferrigno C., 2011, *A&A*, 532, A126
- Koldoba A. V., Lovelace R. V. E., Ustyugova G. V., Romanova M. M., 2002, *ApJ*, 123, 2019
- Koteswara Rao V., Agrawal P. C., Sreekumar P., Thyagarajan K., 2009, *Acta Astronaut.*, 65, 6
- Kreykenbohm I., Coburn W., Wilms J., Kretschmar P., Staubert R., Heindl W. A., Rothschild R. E., 2002, *A&A*, 395, 129
- Kreykenbohm I., Wilms J., Coburn W., Kuster M., Rothschild R. E., Heindl W. A., Kretschmar P., Staubert R., 2004, *A&A*, 427, 975
- Kulsrud R. M., 2005, *Plasma Physics for Astrophysics*. Princeton Univ. Press, Princeton, NJ
- Litwin C., Brown E. F., Rosner R., 2001, *ApJ*, 553, 788
- Lutovinov A., Tsygankov S., 2008, in Axelsson M., ed., *AIP Conf. Ser. Vol. 1054, Cool Discs, Hot Flows: The Varying Faces of Accreting Compact Objects*. AIP, New York, p. 191
- Makishima K. et al., 1990, *ApJ*, 365, L59
- Melatos A., Phinney E. S., 2001, *PASA*, 18, 421
- Mignone A., Bodo G., Massaglia S., Matsakos T., Tesileanu O., Zanni C., Ferrari A., 2007, *ApJS*, 170, 228
- Mihara T. et al., 2007, *Prog. Theor. Phys. Suppl.*, 169, 191
- Mouschovias T. C., 1974, *ApJ*, 192, 37
- Nishimura O., 2005, *PASJ*, 57, 769
- Nishimura O., 2011, *ApJ*, 730, 106
- Payne D. J. B., Melatos A., 2004, *MNRAS*, 351, 569 (PM04)
- Payne D. J. B., Melatos A., 2007, *MNRAS*, 376, 609
- Pottschmidt K. et al., 2005, *ApJ*, 634, L97
- Poutanen J., Beloborodov A. M., 2006, *MNRAS*, 373, 836
- Poutanen J., Gierliński M., 2003, *MNRAS*, 343, 1301
- Press W. H., Teukolsky S. A. T., Vetterling W., Flannery B. P., 1993, *Numerical Recipes in C*. Cambridge Univ. Press, Cambridge
- Reig P., Coe M. J., 1999, *MNRAS*, 302, 700
- Rodes-Roca J. J., Torrejón J. M., Kreykenbohm I., Martínez Núñez S., Camero-Arranz A., Bernabéu G., 2009, *A&A*, 508, 395
- Romanova M. M., Ustyugova G. V., Koldoba A. V., Wick J. V., Lovelace R. V. E., 2003, *ApJ*, 595, 1009
- Schönherr G., Wilms J., Kretschmar P., Kreykenbohm I., Santangelo A., Rothschild R. E., Coburn W., Staubert R., 2007, *A&A*, 472, 353
- Sokolov A. A., Ternov I., 1968, *Synchrotron Radiation*. Pergamon, New York
- Staubert R., Shakura N. I., Postnov K., Wilms J., Rothschild R. E., Coburn W., Rodina L., Klochkov D., 2007, *A&A*, 465, L25
- Suchy S. et al., 2008, *ApJ*, 675, 1487
- Tsygankov S. S., Lutovinov A. A., Serber A. V., 2010, *MNRAS*, 401, 1628
- Vigeliu M., Melatos A., 2008, *MNRAS*, 386, 1294

APPENDIX A: SOLVING THE GS EQUATION

A1 The numerical algorithm

We express the GS equation in non-dimensional form by scaling the physical parameters with $L_0 = R_p = 1$ km, $\rho_0 = 10^6$ g cm $^{-3}$ and $B_0 = 10^{12}$ G. The flux function is normalized to the value at $r = R_p$: $u = \psi/\psi_p$ ($\psi_p = B_0 R_p^2/2$). We perform a variable transformation $x = r^2$ and solve the GS equation on a $(x - y)$ grid which are the normalized $(r^2 - z)$ coordinates. The result is then transformed back

to the $(r - z)$ grid by spline interpolation. With this transformation and scaling, the GS equation for an adiabatic gas reads as

$$4x \frac{\partial^2 u}{\partial x^2} + \frac{\partial^2 u}{\partial y^2} = -Cx(Y_0 - y)^\alpha \frac{dY_0(u)}{du}, \quad (\text{A1})$$

where $C = 16\pi Ag L_0^{1+\alpha}/B_0^2$, $\alpha = 1/(\gamma - 1)$ and $Y_0(u)$ is the mound height profile expressed in scaled flux coordinate u .

We adopt the following set of boundary conditions.

(i) $\psi = \psi_d$ at $z = 0 \forall r$. Here, $\psi_d = B_0 r^2/2$ is the initial guess, which is ψ for a uniform field $\mathbf{B} = B_0 \hat{z}$ (an approximation of the dipolar field in the polar cap region). This is the line-tying condition of the field at the base (Hameury et al. 1983).

(ii) $\psi = \psi_d$ at $r = 0 \forall z$.

(iii) $\psi = \psi_d$ at $r \rightarrow \infty \forall z$. The field is undistorted for $r \gg R_p$. Ideally, one should keep the $r = r_{\text{max}}$ boundary at infinity to fully capture the distortion of the field lines resulting from the lateral pressure of the confined plasma. To implement this numerically is impractical. In our GS solver, the boundary along the radial direction is chosen at $r_{\text{max}} = r_p$, where $\psi = \psi_d$ is fixed as the boundary condition. The mound height profiles considered for the GS solver fall off with radius vanishing at $r = r_p$. Thus, at the $r = r_p$ boundary, there is very little deviation from the initial unloaded field configuration. Possible limitations of this are discussed in Section 3.3.

(iv) $\psi = \psi_d$ at $z \rightarrow \infty$. The field is undistorted for $z \rightarrow \infty$. Setting boundary height (z_{top}) too close to the maximum height of the mound (Z_c) affects the solution and gives an incorrect result. It is seen that setting $z_{\text{top}} \geq 1.5Z_c$ is sufficient for the solution to be stable. Further change in the boundary height (z_{top}) does not change the solution significantly.

We adopt a numerical scheme similar to the one followed by Mouschovias (1974) and Payne & Melatos (2004). The density is determined from the mound height profile and equation (7). A two-state iterative scheme using an outer under-relaxation scheme and an inner successive over-relaxation (SOR) method using Chebyshev acceleration (Press et al. 1993) is adopted to tackle the non-linear source term on the right-hand side. We start with an initial guess solution ($\psi_{\text{ini}} = \psi_d$). The SOR loop converges when $\xi \leq \epsilon_{\text{sor}} \xi_{\text{ini}}$, where ξ is the residue of the differenced equation (left-hand side-right-hand side) (Press et al. 1993), ξ_{ini} is the initial residue at the start of the GS iterations and ϵ_{sor} is the error tolerance for the SOR scheme. The solution from the SOR at the i th GS iteration is then evolved by an under-relaxation scheme

$$\left. \begin{aligned} \Delta &= \psi^i - \psi^{i-1}, \\ \psi_{\text{new}}^i &= \psi^i - \zeta \Delta, \end{aligned} \right\} \quad (\text{A2})$$

where $\zeta \leq 1$ is the under-relaxation parameter. The convergence is considered to be achieved when maximum error at each grid point is reduced below the threshold

$$\frac{\psi^i - \psi^{i-1}}{\psi^{i-1}} < \epsilon_{\text{GS}}. \quad (\text{A3})$$

Smaller values of ζ gave faster convergence but convergence rate did not improve much with ζ below an optimum value ~ 0.01 . The convergence rate depends on the model being used. Cases for which physical parameters (magnetic field, pressure etc.) are near regions where the solution does not exist (see Section 3.3), the GS loop takes longer time to converge. Otherwise, convergence is reached within fewer than 100 steps. Fig. A1 shows mean error $[\sum_{N_x, N_y} (\Delta/N_x N_y)]$ at each step of the iteration for 100 steps. The convergence was reached after nine steps in this case. The error

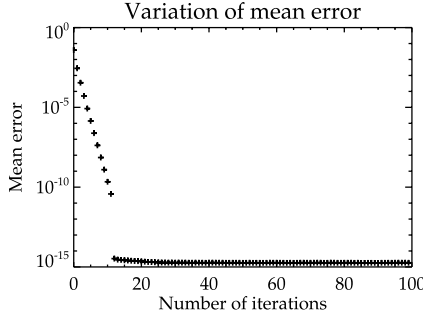


Figure A1. Mean error versus number of iterations of the GS solver until 100 iterations. Convergence (equation A2) was reached after nine steps.

tolerance limits were usually set at $\epsilon_{\text{sor}} = 10^{-8}$ and $\epsilon_{\text{GS}} = 10^{-7}$ for a grid of 1024×1024 .

A2 Testing the GS solver

Our GS solver was tested by comparing results with analytical solutions of the GS equation. We solved the Soloviev equation

$$\Delta^2 \psi = r^2, \quad (\text{A4})$$

whose analytical solution is $\psi_{\text{ana}} = r^2 z^2 / 2$. The maximum absolute difference of the solution from the GS solver and the analytic expression was

$$\left| \frac{\psi_{\text{num}} - \psi_{\text{ana}}}{\psi_{\text{ana}}} \right| \leq 9.85 \times 10^{-5}, \quad (\text{A5})$$

which we consider acceptable.

We also tested the equilibria by using the MHD code *PLUTO* (Mignone et al. 2007) and checking if the solution is stationary with time. The typical Alfvén time-scale of the accreted mound with a scalelength $L_0 = 1$ km, density $\rho_0 = 10^6 \text{ g cm}^{-3}$ and magnetic field $B_0 = 10^{12} \text{ G}$ is $t_A = L_0 / V_A \sim 3.5 \times 10^{-4} \text{ s}$ (V_A is the Alfvén velocity). The solution from the GS solver was put as an initial condition in *PLUTO* with a simulation region located inside the density mound. At the boundary, values of the physical parameters (pressure, magnetic field and density) were kept fixed to the initial value obtained from the GS solution. The simulation was run for several Alfvén times and the solution was found to be stationary. This confirms that the solution obtained from our GS solver represents an equilibrium.

APPENDIX B: GEOMETRY OF HOTSPOT WITH RESPECT TO LINE OF SIGHT (LOS)

Fig. B1 shows the relative position of the hotspot with respect to the observer and the neutron star. We define the frame (X, Y, Z) with origin at the centre of the neutron star (O) such that X'' and X are in the same direction and the angle between Z and Z'' is η_p . The coordinates of the LOS with respect to the origin O are (i, ω) with ω measured from the Y -axis. The unit vector along the LOS is $\hat{n}_\psi \equiv (\sin i \sin \omega, \sin i \cos \omega, \cos i)$. The hotspot lies on the surface of the star with its centre at O' whose coordinates with respect to the O are (R_s, η_p) (see Fig. B1), Z'' being the normal through O' . The GS computation is done in a cylindrical coordinate system (ρ, ϕ, ξ) in the frame (X'', Y'', Z'') , where the angle ϕ is defined with respect to X'' . Coordinates of a point in the (X'', Y'', Z'') frame are $(\rho \cos \phi, \rho \sin \phi, \xi)$.

To express the coordinates of a point on the hotspot in the (X, Y, Z) frame, we first rotate the (X'', Y'', Z'') frame about X'' by an

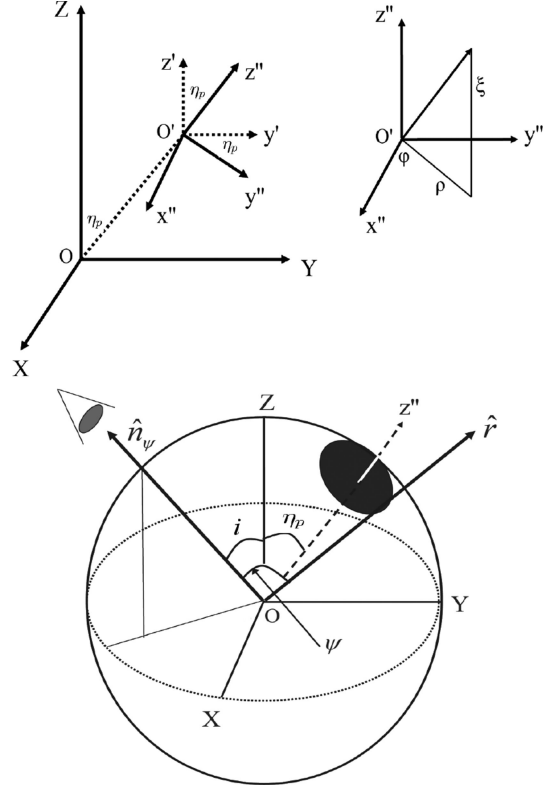


Figure B1. The position and orientation of the coordinate system local to the hotspot (X'', Y'', Z'') with respect to the global coordinate system (X, Y, Z) defined in the frame of the neutron star. The Z axis is the axis of rotation and Z'' is along the magnetic pole O' (which is also the centre of the hotspot). The magnetic axis (Z'') is at an angle η_p to the spin axis (Z). The LOS makes angle i with the Z axis and ω (phase) with the Y axis. In the frame (X'', Y'', Z'') , (ρ, ϕ, ξ) are the cylindrical coordinates where angle ϕ is measured with respect to the X'' axis. The X and X'' axes are in the same direction.

angle η_p to (X', Y', Z') such that Z' is parallel to Z , and then shift the origin from O' to O by distance R_s along the radial line joining OO' . Thus, we get the coordinates of a point \mathbf{r} on the hotspot as $\mathbf{r} \equiv \{\rho \cos \phi, \rho \cos \eta_p \sin \phi + (\xi + R_s) \sin \eta_p, (\xi + R_s) \cos \eta_p - \rho \sin \eta_p \sin \phi\}$, where $r = (\rho^2 + (\xi + R_s)^2)^{1/2}$ is the radial distance of (x, y, z) from O . The angle between the LOS (\hat{n}_ψ) and the radius vector to a point on the hotspot is $\cos \psi = \hat{n}_\psi \cdot \mathbf{r} / r$. The ray coming towards the observer along an LOS is deviated from its local direction of emission on the neutron star surface (\hat{n}_α ; see Fig. B2) due to gravitational bending of light. The local emission angle (α) and the angle between the LOS and the radius vector $\hat{\mathbf{r}}$ can be related by the approximate formula given by Beloborodov (Beloborodov 2002; Poutanen & Beloborodov 2006):

$$\cos \alpha \simeq u + (1 - u) \cos \psi, \quad (\text{B1})$$

where $u = r_s / r$, r_s being the Schwarzschild radius. Since the unit vectors \hat{n}_α , \hat{n}_ψ and $\hat{\mathbf{r}}$ lie in the same plane, we can write $\hat{n}_\alpha \times (\hat{n}_\psi \times \hat{\mathbf{r}}) = C \hat{n}_\alpha \times (\hat{n}_\psi \times \hat{\mathbf{r}})$, C being a constant, as the two vectors lie in the same direction differing only in magnitude. Using $\hat{n}_\alpha \cdot \hat{\mathbf{r}} = \cos \alpha$, the constant C is evaluated to be $C = \sin \alpha / \sin \psi$, for $\alpha \neq 0$. So, \hat{n}_α can be related to \hat{n}_ψ (as in Poutanen & Gierliński 2003)

$$\hat{n}_\alpha = \frac{\sin(\psi - \alpha)}{\sin \psi} \hat{\mathbf{r}} + \frac{\sin \alpha}{\sin \psi} \hat{n}_\psi. \quad (\text{B2})$$

For $\alpha = 0$ (which corresponds to $\psi = 0$ from equation B1), we have $\hat{n}_\alpha = \hat{n}_\psi = \hat{\mathbf{r}}$. A numerical computation of $\sin(\psi - \alpha) / \sin \psi$ and

